ResearchGate

See discussions, stats, and author profiles for this publication at: https://www.researchgate.net/publication/349048970

Fano-resonant ultrathin film optical coatings

Article *in* Nature Nanotechnology · April 2021

DOI: 10.1038/s41565-020-00841-9

CITATIONS
64

READS
1,984

11 authors, including:

Mohamed Elkabbash
The University of Arizona
92 PUBLICATIONS **2,242** CITATIONS

SEE PROFILE

Sohail Abdul Jalil
University of Ottawa
33 PUBLICATIONS **677** CITATIONS

SEE PROFILE

Jihua Zhang
Songshan Lake Materials Laboratory
89 PUBLICATIONS **1,187** CITATIONS

SEE PROFILE

Michael Hinczewski
Case Western Reserve University
145 PUBLICATIONS **3,238** CITATIONS

SEE PROFILE

All content following this page was uploaded by Sohail Abdul Jalil on 13 September 2021.

The user has requested enhancement of the downloaded file.

nature nanotechnology

ARTICLES

https://doi.org/10.1038/s41565-020-00841-9

Fano-resonant ultrathin film optical coatings

Mohamed ElKabbash[1,2]✉, Theodore Letsou[2], Sohail A. Jalil[1], Nathaniel Hoffman[2], Jihua Zhang[1], James Rutledge[1], Andrew R. Lininger[2], Chun-Hao Fann[1], Michael Hinczewski[2]✉, Giuseppe Strangi[2,3]✉ and Chunlei Guo[1]✉

Optical coatings are integral components of virtually every optical instrument. However, despite being a century-old technology, there are only a handful of optical coating types. Here, we introduce a type of optical coatings that exhibit photonic Fano resonance, or a Fano-resonant optical coating (FROC). We expand the coupled mechanical oscillator description of Fano resonance to thin-film nanocavities. Using FROCs with thicknesses in the order of 300 nm, we experimentally obtained narrowband reflection akin to low-index-contrast dielectric Bragg mirrors and achieved control over the reflection iridescence. We observed that semi-transparent FROCs can transmit and reflect the same colour as a beam splitter filter, a property that cannot be realized through conventional optical coatings. Finally, FROCs can spectrally and spatially separate the thermal and photovoltaic bands of the solar spectrum, presenting a possible solution to the dispatchability problem in photovoltaics, that is, the inability to dispatch solar energy on demand. Our solar thermal device exhibited power generation of up to 50% and low photovoltaic cell temperatures (~30 °C), which could lead to a six-fold increase in the photovoltaic cell lifetime.

In photonics, Fano resonance takes place when two oscillators with different damping rates are weakly coupled, that is, by coupling resonators with narrow (weakly damped) and broad (strongly damping) spectral lines[1]. Although individual Mie scatterers exhibit a subtle Fano resonance near their plasmonic or polaritonic resonance[1,2], a clear Fano resonance is observed in the extinction of coupled plasmonic nanostructures with multiple spectrally overlapping resonances and different damping rates. This is realized, for instance, by coupling a radiatively broad bright mode and a spectrally narrow dark mode[3–8]. In metamaterials, Fano resonance was demonstrated in the reflection of asymmetric split-ring resonators, an observation arising from the interference between narrowband magnetic dipole and broadband electric dipole modes[6,9]. A high quality factor Fano resonance has been demonstrated in all-dielectric metasurfaces[10]. The steep dispersion associated with Fano resonances and their relatively high quality factors promise various applications in lasing, structural colouring[11], slow-light devices[1,12], optical switching and bistability[13], biosensing[14], ultrasensitive spectroscopy[15], non-linear optical isolators[16] and image processing[17]. In addition, Fano resonance morphs into electromagnetic-induced transparency when the energy levels of both broad and narrow resonance coincide[1,18,19]. However, demonstrations of Fano resonance in nanophotonic devices typically require time-consuming and costly nanolithography fabrication techniques, for example, electron-beam lithography or focused ion beam milling[7], which limits their utility from a technological perspective.

On the other hand, optical coatings represent a century-old class of optical elements that are integral components of nearly every optical instrument[20]. Their applications span many branches of science and technology, including lasers[21], astronomy[22], displays and lighting[23,24], anti-counterfeiting[25], radiative cooling[26–28], photovoltaics[29], structural colouring[30–33], smart windows[34] and the UV protection and anti-glare coatings used in eyeglasses[35], to name a few[20,36].

Here, we introduce a thin-film optical coating that exhibits photonic Fano resonance. The optical coating consists of a broadband light absorber, representing the continuum, weakly coupled to a narrowband light absorber, representing the discrete state. In this study we first developed an analytical model for Fano-resonant optical coatings (FROCs) based on coupled oscillator theory. Then, we investigated the optical properties of FROCs, comparing them with other commonly used optical coatings. We have identified a unique property of semi-transparent FROCs, namely that they can behave as beam-splitting colour filters. Finally, we experimentally demonstrated efficient hybrid solar thermal/electric energy generation using FROCs.

Figure 1a schematically shows the main types of thin-film optical coatings. A metallic film deposited on a transparent substrate (Fig. 1a(i)) serves as a mirror or as a beam splitter by controlling the film thickness. An anti-reflective coating (Fig. 1a(ii)) suppresses reflection and consists of a dielectric film deposited on a higher-index dielectric substrate in its simplest form. A dielectric (Bragg) mirror consists of multiple dielectric thin films with quarter-wavelength thickness and different refractive indices (Fig. 1a(iii)). More recently, attention has been given to thin-film optical absorbers as they provide a large-scale and inexpensive alternative to complex and lithographically intense nano-resonators, metamaterials and metasurfaces for controlling light absorption[31–33] and thermal emission beyond the intrinsic absorption or emission[37,38] of materials. A simple broadband light absorber cavity consists of an ultrathin dielectric film with strong optical losses deposited on a highly reflective metallic substrate[32] or a lossless dielectric on an absorptive substrate (Fig. 1a(iv))[31]. A simple narrowband light absorber cavity consists of a metal–dielectric–metal (MDM) cavity that has been shown to be an absorption filter for structural colouring[30,33] and gas sensing (Fig. 1a(v))[39,40]. When a broadband light absorber cavity is weakly coupled to a narrowband light absorber cavity (Fig. 1a(vi)) resonant destructive interference between the spectrally overlapping cavities yields asymmetric Fano resonance absorption and reflection lines.

Coupled oscillator theory for thin-film optical coatings

The coupled mechanical oscillator model is used extensively to model Fano resonances[41]. Here, we extended the coupled oscillator

[1]The Institute of Optics, University of Rochester, Rochester, NY, USA. [2]Department of Physics, Case Western Reserve University, Cleveland, OH, USA. [3]CNR Nanotec and Department of Physics, University of Calabria, Rende, Italy. ✉e-mail: melkabba@ur.rochester.edu; mxh605@case.edu; giuseppe.strangi@case.edu; guo@optics.rochester.edu

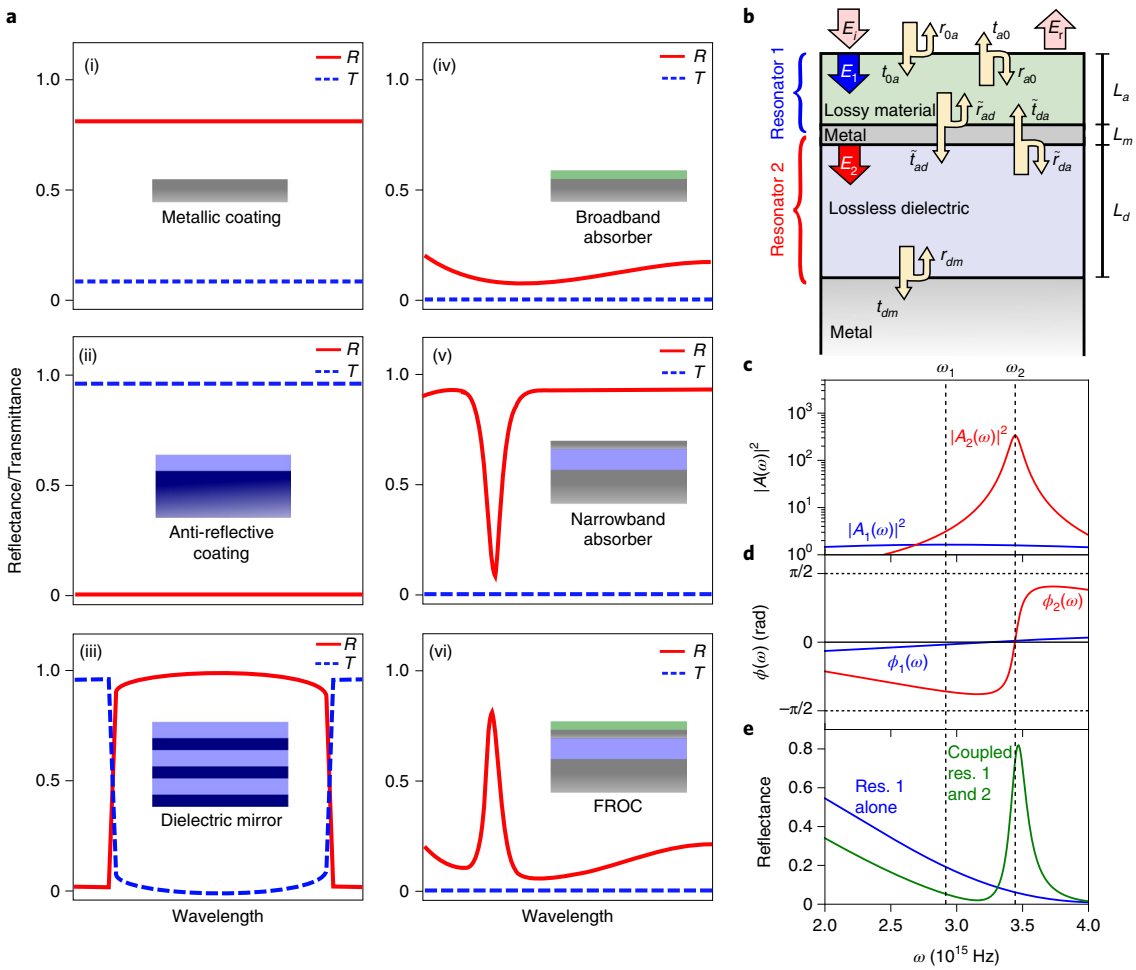

Fig. 1 | Fano resonance in thin-film optical coatings. a, Schematics of the reflectance R and transmittance T of the main types of optical coatings, including metallic coatings used as mirrors and beam splitters (i), anti-reflective dielectric coatings (ii), dielectric (Bragg) mirrors (iii), broadband optical absorbers (iv), narrowband absorbers (v) and the proposed FROC coating (vi). **b**, Schematic of the structure of a FROC consisting of two weakly coupled resonators where resonator 1 (the top two layers consisting of lossy material and metal) represents a broadband absorber and resonator 2 (layers 2 to 4 consisting of metal, dielectric and metal) represents a narrowband absorber. The two resonators share a metal layer that determines their coupling strength. **c**, The calculated oscillator intensities $|A_i(\omega)|^2$ $(i = 1, 2)$. The resonant frequencies ω_i are indicated by dashed lines. **d**, The corresponding oscillator phases $\Phi_i(\omega)$. **e**, The reflectance from the whole system of two coupled resonators (green). For contrast, the reflectance of just resonator 1 (lossy material on a metal substrate) is shown in blue.

theory to thin-film optical coatings[1,42] (for the detailed derivation, see Methods). A schematic of a FROC is shown in Fig. 1b: resonator 1 consists of a lossy material of thickness L_a and complex refractive index $n_a = n_a^{Re} + in_a^{Im}$, followed by a metal of thickness L_m and complex refractive index $n_m = n_m^{Re} + in_m^{Im}$, where Re and Im stand for real and imaginary parts, and i is the unit imaginary number. Resonator 2 is an MDM cavity[43] consisting of a thin metallic film with thickness L_m, a lossless dielectric with thickness L_d and refractive index n_d, and an optically opaque metallic substrate. The total electric fields within the first and second resonators are E_1 and E_2, respectively. We define the intensity ratio A_k as the ratio of the field inside the kth resonator (E_k) to the field injected into the kth resonator (E_k^i), that is, $A_k = (E_k/E_k^i)$. These ratios are given by:

$$A_1(\omega) \approx \frac{1}{1 - |r_{a0}r_{am}|e^{-2Im[\phi_a(\omega)]}e^{i\{2Re[\phi_a(\omega)]+\phi_{a0}+\phi_{am}\}}}, \quad (1)$$

and

$$A_2(\omega) \approx \frac{1}{1 - |r_{dm}|^2 e^{2i[\phi_d(\omega)+\phi_{dm}]}}. \quad (2)$$

Figure 1c shows the calculated oscillator intensities $|A_k(\omega)|^2$ for the sample material parameters described in the Methods. The resonant frequencies ω_i are indicated by dashed lines. The oscillator phases $\Phi_i(\omega)$, defined by $A_i(\omega) = |A_i(\omega)|\exp[i\Phi_i(\omega)]$, are shown in Fig. 1d. Note that the phase of the strongly damped oscillator (resonator 1) varies slowly, whereas the phase of the weakly damped oscillator (resonator 2) changes by ~π at resonance. When the two resonators are coupled and resonator 1 is driven by a field incident from the superstrate E_i, we can express the total field injected into resonator 1 as $E_{1i} = t_{0a}E_i + E_{2i}r_{dm}\tilde{t}_{da}r_{a0}e^{i[2\phi_d(\omega)+\phi_a(\omega)]}$. In turn, the field in resonator 2 exists due to the field from resonator 1 propagating downward through the spacer and is given by $E_{2i} = E_1\tilde{t}_{ad}e^{i\phi_a(\omega)}$. Here, $\tilde{t}_{ad}$ and $\tilde{t}_{da}$ represent transmission coefficients across the metal spacer layer (Fig. 1b and Methods). These relationships can be expressed in the following matrix equation for E_1 and E_2:

$$\begin{pmatrix} \frac{1}{A_1(\omega)} & -r_{dm}\tilde{t}_{da}r_{a0}e^{i[2\phi_d(\omega)+\phi_a(\omega)]} \\ -\tilde{t}_{ad}e^{i\phi_a(\omega)} & \frac{1}{A_2(\omega)} \end{pmatrix} \begin{pmatrix} E_1 \\ E_2 \end{pmatrix} = \begin{pmatrix} t_{0a}E_i \\ 0 \end{pmatrix}. \quad (3)$$

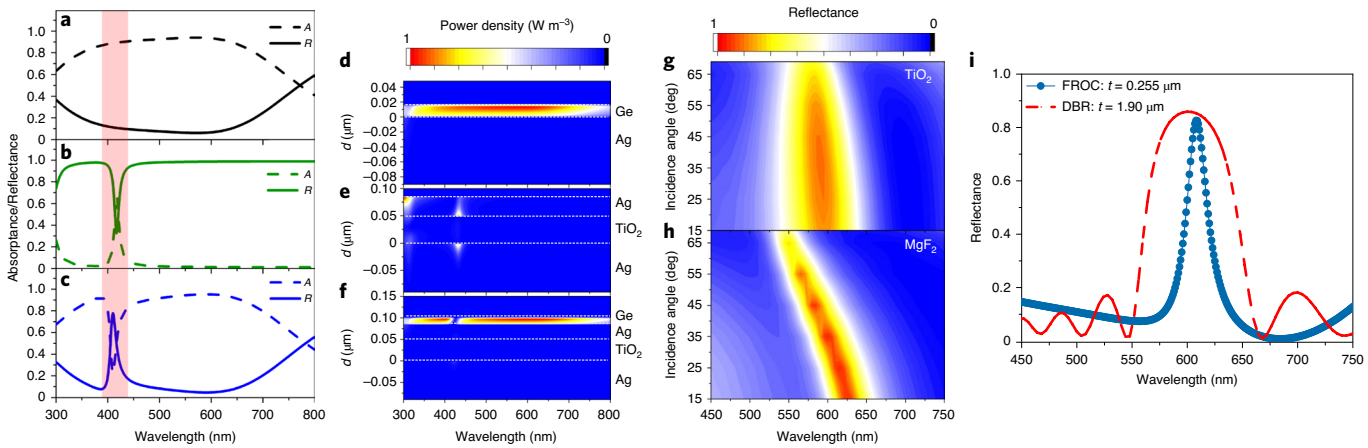

Fig. 2 | Demonstration and properties of Fano-resonant optical coatings. a–c, Calculated reflectance and absorptance A of a thin-film broadband light absorber (**a**), a narrowband light absorber (**b**) and a FROC (**c**). The highlighted region shows the spectral range where the narrowband light absorber resonance and Fano resonance take place. **d–f**, The calculated normalized power dissipation density in the three structures, highlighting the resonant destructive interference between the broadband and narrowband nanocavities. **g**,**h**, The measured angular reflection of a FROC with a high-index dielectric (TiO_2; **g**) and a FROC with a low-index dielectric (MgF_2; **h**). **i**, The calculated reflectance from a low-index contrast dielectric Bragg reflector with thickness $t = 1.9\,\mu m$ compared with the selective reflection of a FROC ($t = 0.255\,\mu m$).

The coupling between E_1 and E_2 occurs through the off-diagonal terms in the matrix. Equation (3) enables us to obtain the reflectance from the coupled oscillator, shown in Fig. 1e. The coupled oscillator reflectance shows a narrow reflection band that exhibits the asymmetric Fano line shape with a peak occurring at $\sim\omega_2$. Note that for $\tilde{t}_{ad}$ and $\tilde{t}_{da} \rightarrow 0$, that is, for an optically opaque top metal film, that is, when the cavities are decoupled ($L_m \rightarrow \infty$), the off-diagonal terms vanish and the Fano resonance disappears (Supplementary Fig. 1).

Demonstration and properties of FROCs

Figure 2a–c shows the reflectance and absorptance of a broadband absorber, narrowband absorber and FROC, respectively, calculated using the transfer matrix method. The broadband absorber (Fig. 2a) consists of a 15-nm Ge film on a 100-nm Ag film [Ge (15 nm)–Ag (100 nm)] with an absorption band full-width at half-maximum (FWHM) of ~600 THz. The narrowband absorber (Fig. 2b) consists of a Ag (30 nm)–TiO_2 (50 nm)–Ag (100 nm) MDM cavity producing an absorption line with a FWHM of ~15 THz. Figure 2c shows the calculated reflection and absorption of a FROC (Ge (15 nm)–Ag (30 nm)–TiO_2 (50 nm)–Ag (100 nm)). The FROC in Fig. 2c is realized by overlapping the broadband absorber, which represents a continuum with a nearly constant phase, and a narrowband absorber, with a rapid phase shift near resonance (Supplementary Fig. 2). The Fano resonance linewidth can be controlled by controlling the damping in the second resonator (Γ_2; see Methods and Supplementary Figs. 3 and 4). The FROC produces broadband absorption except at wavelengths corresponding to the MDM cavity resonance where it shows an asymmetric (Fano) reflection and absorption lines (Supplementary Fig. 5). Figure 2d–f show the calculated power dissipation densities corresponding to the optical coatings presented in Fig. 2a–c, respectively (see Methods). For the broadband absorber (Fig. 2d), the incident light is trapped inside the absorbing Ge film[40]. Similarly, when the MDM cavity is at resonance, light is trapped inside the cavity and dissipated in the metallic mirrors (Fig. 2e). By overlapping the two optical coatings, resonant destructive interference between the two resonators takes place and light escapes both resonators (Fig. 2f).

The iridescence of the selective reflection can be controlled by judiciously choosing the dielectric film in the MDM cavity[33] (see Methods). Figure 2g,h shows the measured angular reflection spectra of p-polarized light from a high-index dielectric FROC (Ge (15 nm)–Ag (20 nm)–TiO_2 (100 nm)–Ag (100 nm)) and a low-index dielectric FROC (Ge (15 nm)–Ag (20 nm)–MgF_2 (180 nm)–Ag (100 nm)), respectively (for s-polarized angular reflection, see Supplementary Fig. 6). The refractive indices of TiO_2 and MgF_2 are ~2.2 and 1.35, respectively. The reflectance of the high-index FROC is angle-independent over a wide angular range (±70°), whereas the low-index FROC is highly iridescent. Iridescent structural colours are important for the anti-counterfeiting measures used in many currencies and also for spectral splitting of the solar spectrum (Supplementary Fig. 7)[25]. For most structural colouring applications, however, iridescence is problematic[44] and a high-index FROC is more suitable[44].

The observed selective reflection is reminiscent of dielectric mirrors, for example, distributed Bragg reflectors (DBRs). Although dielectric mirrors are used as high-reflection coatings, their selective reflection properties make them attractive for structural colouring and single-frequency lasers[45,46]. The bandwidth of a DBR mirror is inversely proportional to the difference in refractive index of its two constituent dielectrics. Similarly, the required number of periods to achieve high reflection is inversely proportional to the difference in index. Figure 2i shows the calculated reflectance for a DBR mirror and a FROC. The DBR consists of ten Al_2O_3–SiO_2 bilayers with an overall thickness of 1.9 μm and a FWHM of ~100 nm, and the FROC consists of Ge (15 nm)–Ag (35 nm)–TiO_2 (105 nm)–Ag (100 nm) with an overall thickness of 0.255 μm and a FWHM of ~30 nm. Accordingly, FROCs can provide narrowband selective reflectance with a thickness an order of magnitude less than DBR mirrors. The high dispersion associated with Fano resonance leads to a high effective group index which is promising for slow-light applications[12] (Supplementary Fig. 8).

FROCs as beam splitter filters

FROCs enjoy a unique property unattainable by existing thin-film optical coatings, namely they act as beam splitter filters (BSFs), that is, they transmit and reflect the same colour under white light illumination (for comparison with other beam splitters, see Supplementary Fig. 9). Figure 3a shows the calculated reflection and transmission of an MDM cavity consisting of Ag (20 nm)–TiO_2(85 nm)–Ag (20 nm). The MDM cavity acts as a transmission filter such that the reflection minimum corresponds to the transmission maximum. Figure 3b shows the calculated reflection and

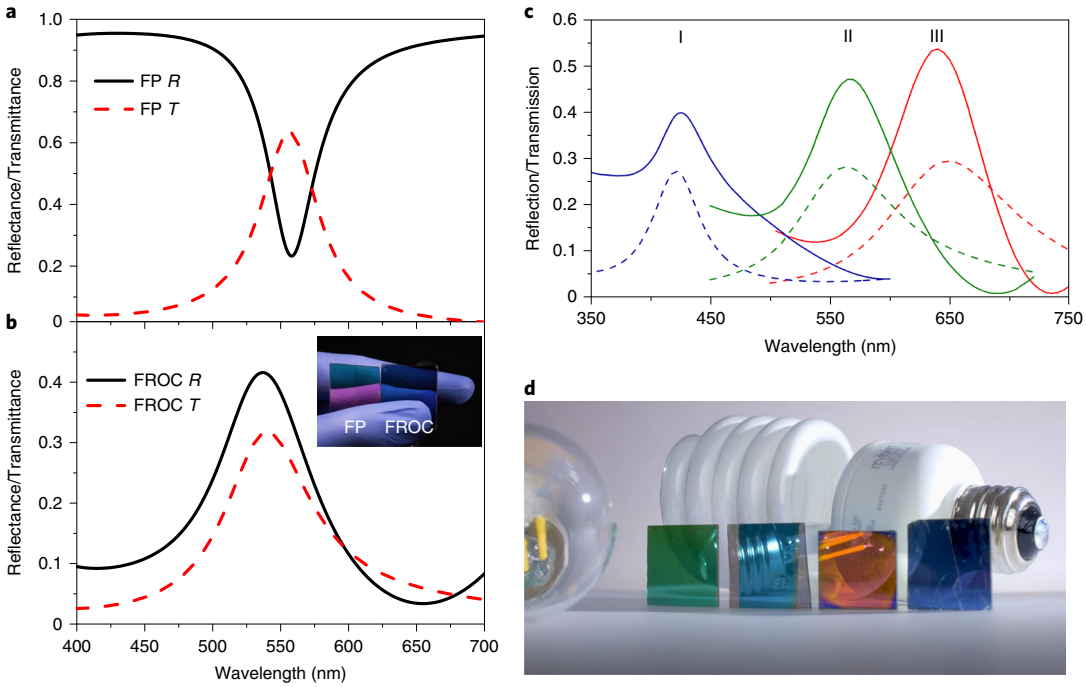

Fig. 3 | FROC as a beam splitter filter. a,**b**, Calculated reflectance and transmittance of a transmission filter based on an Fabry–Perot (FP) cavity consisting of a metal–dielectric–metal stack. (**a**) and a BSF-FROC (**b**). The reflectance and transmittance are complementary for the MDM cavity, whereas for the FROC, both reflectance and transmittance peaks overlap. The inset in **b** shows a photograph of a conventional transmission filter and a BSF-FROC. The former reflects red while transmits green. The FROC, however, reflects and transmits the same blue colour. **c**, Measured transmittance (dashed lines) and reflection (solid lines) for three BSF-FROCs (Ge (15 nm)–Ag (25 nm)–PMMA (I, 100 nm; II, 120 nm; III, 170 nm)–Ag (25 nm)). **d**, Photograph of BSF-FROCs showing their potential for the structural colouring of transparent objects. The reflection of the incandescent bulb and transmission from the fluorescent light bulb have the same colour for each BSF-FROC filter.

transmission for a FROC with semi-transparent metallic films consisting of Ge (15 nm)–Ag (20 nm)–TiO_2 (85 nm)–Ag (20 nm), for which the peak transmission and peak reflection overlap within the visible range, that is, the FROC behaves as a BSF. The inset of Fig. 3b shows a photograph of a transmission filter and a BSF-FROC. The transmission filter reflects and transmits different colours (red and green, respectively), whereas the BSF-FROC reflects and transmits the same blue colour (Supplementary Fig. 10). Figure 3c shows the measured reflection and transmission (incidence angle is 15°) from three BSF-FROCs (Ge (15 nm)–Ag (25 nm)–PMMA (I, 100 nm; II, 120 nm; III, 170 nm)–Ag (25 nm); PMMA, poly(methyl methacrylate)). Clearly, the reflection and transmission peaks overlap for each BSF. Figure 3d presents a photograph of four BSF-FROCs showing that the reflection of the incandescent bulb and transmission from the fluorescent light bulb have the same colour. This property is particularly interesting for the structural colouring of transparent objects as it provides a similar effect to pigment-based colouring of transparent objects such as glass.

Solar hybrid thermal-electric power generation using FROCs

Hybrid thermal-electric power (HTEP) generation is a solar energy generation approach that has recently gained attention[47–50]. The goal is to divide the solar spectrum into a photovoltaic (PV) band, with photon energy larger than or approximately equal to the bandgap energy E_g guided towards a PV cell, while directing the rest of the solar spectrum to a solar absorber to be converted into thermal energy (thermal bands). For single-junction PV cells, however, photons with energy $<E_g$ are wasted, which is a major source of the Shockley–Queisser efficiency limit. In addition, photons with energy $<E_g$ or $\gg E_g$ heat up the PV cell, which decreases the efficiency by ~0.5% per 1 °C[51] and increases the aging rate of PV cells, with the rate nearly doubling with every 10 °C increase in temperature[52]. On the other hand, HTEP takes advantage of the strengths of PV and concentrated solar power energy generation: PV energy is efficient but solar thermal energy can be stored at low cost for night-time dispatchment, or can be used directly for solar thermal application, for example, water heating, sanitation or desalination[53] (see Supplementary Figs. 11–13 for more details on HTEP vs solar thermophotovoltaics and concentrated solar power generation). Addressing night-time dispatchment is crucial to deal with the duck curve and curtailment problem, that is, the mismatch between peak solar energy (midday) production and peak energy demand (sunset), which forces grid managers to curtail solar energy sources by switching off solar panels[54].

A major practical challenge for hybrid thermal-electric systems, however, is finding feasible optical materials that can effectively divide the solar spectrum into the desired PV and thermal bands[48,49]. Figure 4a shows a conventional hybrid PV/solar-thermal energy conversion strategy in which the incident solar spectrum is concentrated on a spectrum splitter that directs sub-bandgap photons ($<E_g$) to a thermal receiver and reflects photons with energies $>E_g$ to a PV cell[49]. A quad-band spectrum-splitting filter has been reported that divides the solar spectrum into a PV band, two thermal bands and an infrared band, with the filter itself having low emissivity[55]. The optical filter consisted of a dielectric mirror on a cermet selective solar absorber. However, this approach suffers from the high cost of depositing dielectric mirrors that are usually tens of micrometres thick[47]. Moreover, optical concentration is required to economically justify the use of dielectric mirrors. Dielectric mirrors, however, do not operate efficiently under optical concentration due to their strong angular sensitivity[47].

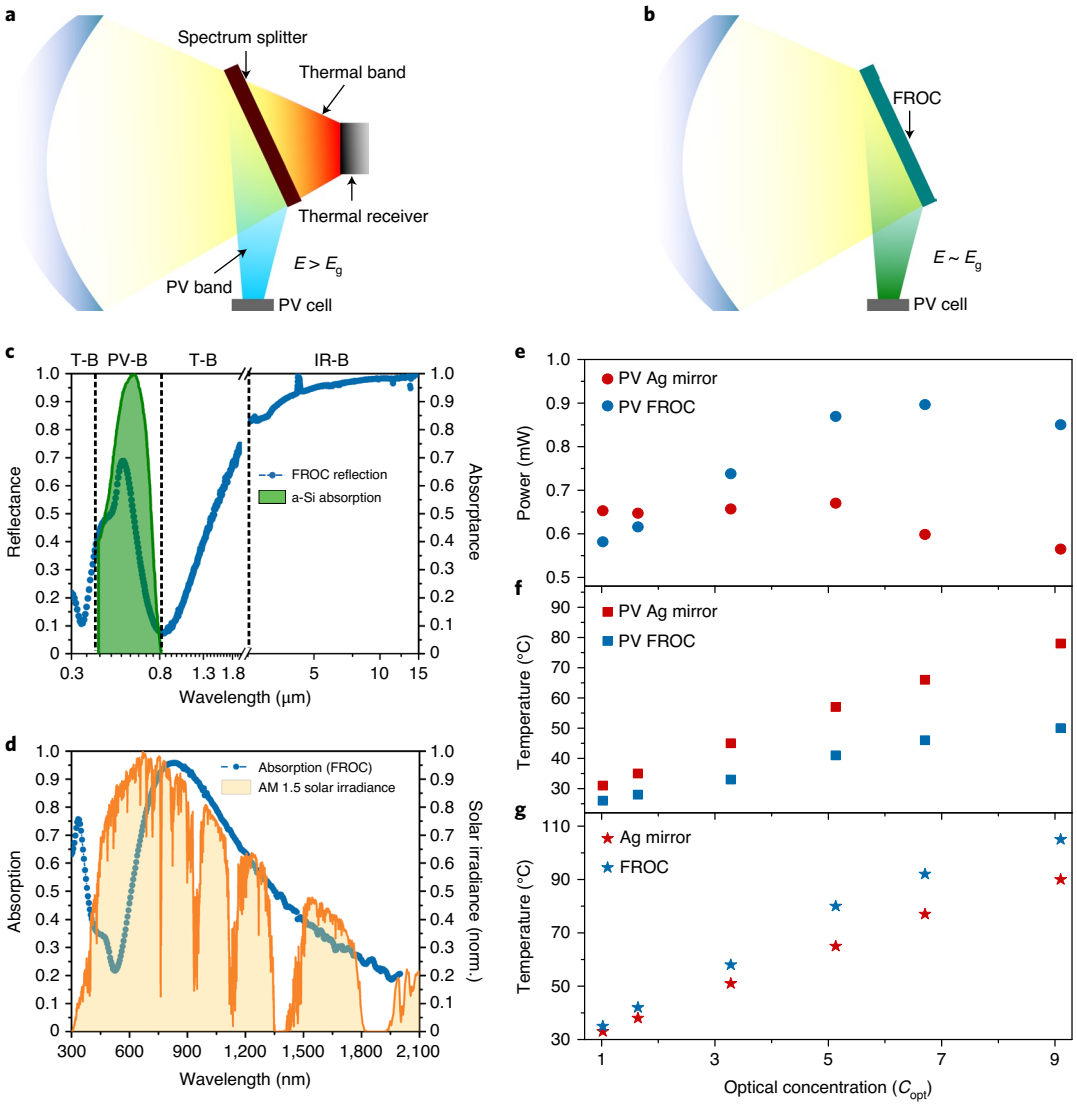

Fig. 4 | FROCs for hybrid thermal-electric solar energy conversion. a, Schematic of a conventional PV/solar-thermal energy conversion set-up in which concentrated solar light is incident on a spectrum splitting filter that reflects photons with energies greater than the PV bandgap energy E_g to a PV cell while transmitting the rest to a separate thermal receiver. **b**, A FROC, however, can reflect photons with energies close to E_g while directly absorbing photons $\gg E_g$ or $< E_g$. **c**, Measured reflectance of a Ge(15 nm)–Ni(5 nm)–TiO_2(85 nm)–Ag(120 nm) FROC that selectively reflects light within the wavelength range corresponding to the absorptance of an a-Si PV cell (green). T-B, PV-B and IR-B correspond to the thermal band, PV band and infrared band, respectively. **d**, The measured absorption of the same FROC shows overall high average absorption within the solar spectrum. The solar irradiance spectrum (AM 1.5) is shown for reference. **e–g**, For different optical concentrations C_{Opt} we measured the power output from a PV cell receiving light reflected from an Ag mirror and the FROC (**e**), the temperature of the PV cell operating with an Ag mirror and the FROC (**f**) and the temperature of the Ag mirror and the FROC (**g**).

A FROC acts as a monolithic spectrum splitter and a solar absorber. With proper design, a FROC can selectively reflect a wavelength range corresponding to photons with an energy of around E_g and absorb the remainder of the solar spectrum (Fig. 4b). We used a FROC consisting of Ge(15 nm)–Ni(5 nm)–TiO_2(85 nm)–Ag(120 nm). Figure 4c shows the FROC reflection at an incidence angle of 45°, at which the Fano resonance peak overlaps strongly with the amorphous silicon (a-Si) absorption band, that is, the FROC is designed to selectively reflect the PV band of an a-Si PV cell. We designed a FROC spectrum splitter/absorber with four bands: two thermal bands that absorb ultraviolet and near-infrared wavelengths, a PV band that corresponds to wavelengths around the E_g of a-Si PV cell and an infrared band with near zero emissivity to minimize thermal radiation losses in the absorber. Figure 4d shows the measured absorption of unpolarized light incident on the FROC at an incidence angle of 45°. The FROC exhibits strong absorption over the entire solar spectrum with limited absorption beyond the solar spectrum, that is, it behaves as a selective light absorber with average absorptance $\bar{\alpha} \sim 0.55$ (see Methods). Thus, the a-Si PV cell receives photons of $\sim E_g$ only and, ideally, can operate with higher efficiency at higher optical concentrations while the solar energy absorbed by the FROC can be independently used for other solar thermal applications or for energy storage. In addition, the FROC behaves as a selective solar absorber as it has low spectral emissivity $\bar{\varepsilon} \sim 0.0014$ in the infrared wavelength range (Supplementary Fig. 14). The low emissivity suppresses the blackbody radiation losses and increases the optothermal efficiency of the absorber[56,57]. Finally, the weak angle dependence of the FROC with a high-index

dielectric means that it can operate efficiently under optical concentration (Supplementary Fig. 15).

To demonstrate HTEP generation using FROCs experimentally, we used a solar simulator and a lens to provide optical concentration (Supplementary Fig. 16). The incident intensity $I = C_{Opt} I_{Solar}$, where C_{Opt} is the optical concentration and I_{Solar} is the solar radiation intensity and is ~1,000 W m^{-2}. Here, solar light is incident on a reflecting silver mirror or a FROC tilted at an angle of 45° and is then directed to an a-Si PV cell. The temperatures of the Ag mirror, FROC and PV cell were measured using thermocouples (see Methods). At low C_{Opt}, the PV cell generates more power from light reflected from an Ag mirror (Fig. 4e). However, for $C_{Opt} \geq 2$, the PV cell receiving solar light from a FROC generates higher power. This is because for lower C_{Opt}, the higher reflection of the Ag mirror within the PV band outweighs the deterioration of efficiency due to heat generated inside the PV cell. At higher C_{Opt}, however, the elevated temperature reduces the PV efficiency and a PV cell operating with a FROC generates more power. Figure 4f shows that the temperature of a PV cell operating with light reflected from an Ag mirror is consistently higher than that of a PV cell operating with light reflected from a FROC. The temperature difference between the two PV cells at $C_{Opt} = 9$ is ~30 °C, which amounts to a possible six-fold increase in the projected lifetime of the PV cell operating with a FROC. These approaches, however, mitigate the thermally induced efficiency reduction and do not exploit the excess thermal energy. The power generated from the FROC/PV system is ~50% higher than that from the Ag/PV system at $C_{Opt} = 5$. In addition, the temperature of the FROC is higher than the temperature of the silver mirror for all C_{Opt} (Fig. 4g), that is, the unwanted heat inside the PV cell is now generated inside the FROC and can be used for thermal energy storage.

Conclusions

We have presented herein an optical coating that exhibits the photonic Fano resonance (FROC). Two main applications of FROCs have been demonstrated: a beam splitter colour filter that reflects and transmits the same colour, and a spectral filter for hybrid thermal-electric solar power generation. We envision several research directions resulting from our demonstration of the FROC. Improving PV efficiency under one-Sun illumination by increasing the reflectance in the PV band and increasing the stability of the thin-film coating at high temperatures are necessary for some high-temperature solar thermal applications, for example, solar thermophotovoltaics and solar thermoelectric generation[58]. Controlling the parameters of FROCs opens the possibility to realize double and multi-Fano resonances using FROCs as well as the photonic analogue of electromagnetic-induced transparency. Moreover, the demonstration of multiple Fano resonances can be used to create hybrid thermal-electric energy generation while operating a multijunction PV cell. Furthermore, investigating the possible non-linear properties of FROCs could lead to active photonic applications and reconfigurable non-reciprocity[59]. Finally, incorporating a phase-change material into a FROC could lead to tunable optical modulators with high modulation depth and could find applications in steganography[55,60].

Online content

Any methods, additional references, Nature Research reporting summaries, source data, extended data, supplementary information, acknowledgements, peer review information; details of author contributions and competing interests; and statements of data and code availability are available at https://doi.org/10.1038/s41565-020-00841-9.

Received: 6 May 2020; Accepted: 10 December 2020;
Published online: 04 February 2021

References

1. Limonov, M. F., Rybin, M. V., Poddubny, A. N. & Kivshar, Y. S. Fano resonances in photonics. *Nat. Photonics* **11**, 543–554 (2017).
2. Miroshnichenko, A. E. et al. Fano resonances: a discovery that was not made 100 years ago. *Opt. Photonics News* **19**, 48–48 (2008).
3. Giannini, V., Francescato, Y., Amrania, H., Phillips, C. C. & Maier, S. A. Fano resonances in nanoscale plasmonic systems: a parameter-free modeling approach. *Nano Lett.* **11**, 2835–2840 (2011).
4. Mukherjee, S. et al. Fanoshells: nanoparticles with built-in Fano resonances. *Nano Lett.* **10**, 2694–2701 (2010).
5. Zhang, S., Bao, K., Halas, N. J., Xu, H. & Nordlander, P. Substrate-induced Fano resonances of a plasmonic nanocube: a route to increased-sensitivity localized surface plasmon resonance sensors revealed. *Nano Lett.* **11**, 1657–1663 (2011).
6. Luk'yanchuk, B. et al. The Fano resonance in plasmonic nanostructures and metamaterials. *Nat. Mater.* **9**, 707–715 (2010).
7. Fan, J. A. et al. Self-assembled plasmonic nanoparticle clusters. *Science* **328**, 1135 (2010).
8. Verellen, N. et al. Fano resonances in individual coherent plasmonic nanocavities. *Nano Lett.* **9**, 1663–1667 (2009).
9. Fedotov, V. A., Rose, M., Prosvirnin, S. L., Papasimakis, N. & Zheludev, N. I. Sharp trapped-mode resonances in planar metamaterials with a broken structural symmetry. *Phys. Rev. Lett.* **99**, 147401 (2007).
10. Yang, Y., Kravchenko, I. I., Briggs, D. P. & Valentine, J. All-dielectric metasurface analogue of electromagnetically induced transparency. *Nat. Commun.* **5**, 5753 (2014).
11. Shen, Y. et al. Structural colors from Fano resonances. *ACS Photonics* **2**, 27–32 (2015).
12. Khurgin, J. B. Slow light in various media: a tutorial. *Adv. Opt. Photon.* **2**, 287–318 (2010).
13. Miroshnichenko, A. E., Flach, S. & Kivshar, Y. S. Fano resonances in nanoscale structures. *Rev. Mod. Phys.* **82**, 2257–2298 (2010).
14. Ruan, B. et al. Ultrasensitive terahertz biosensors based on Fano resonance of a graphene/waveguide hybrid structure. *Sensors* **17**, 1924 (2017).
15. Wu, C. et al. Fano-resonant asymmetric metamaterials for ultrasensitive spectroscopy and identification of molecular monolayers. *Nat. Mater.* **11**, 69–75 (2011).
16. Sounas, D. L. & Alù, A. Fundamental bounds on the operation of Fano nonlinear isolators. *Phys. Rev. B* **97**, 115431 (2018).
17. Cordaro, A. et al. High-index dielectric metasurfaces performing mathematical operations. *Nano Lett.* **19**, 8418–8423 (2019).
18. Sonnefraud, Y. et al. Experimental realization of subradiant, superradiant, and Fano resonances in ring/disk plasmonic nanocavities. *ACS Nano* **4**, 1664–1670 (2010).
19. Liu, N. et al. Plasmonic analogue of electromagnetically induced transparency at the Drude damping limit. *Nat. Mater.* **8**, 758–762 (2009).
20. Macleod, H. A. *Thin Film Optical Filters*, 4th edn (Adam Hilger, 1986).
21. Gallais, L. & Commandré, M. Laser-induced damage thresholds of bulk and coating optical materials at 1030 nm, 500 fs. *Appl. Opt.* **53**, A186–A196 (2014).
22. Anjum, F., Fryauf, D. M., Ahmad, R., Phillips, A. C. & Kobayashi, N. P. Improving silver mirrors with aluminum oxynitride protection layers: variation in refractive index with controlled oxygen content by radiofrequency magnetron sputtering. *IEEE Spect.* **26**, 34–35 (2018).
23. Tannas, L. E. Flat-panel displays displace large, heavy, power-hungry CRTs. *IEEE Spectr.* **26**, 34–35 (1989).
24. Hornbeck, L. J. Digital light processing for high-brightness high-resolution applications. In *Proc. SPIE 3013, Projection Displays III* (SPIE, 1997).
25. Dobrowolski, J. A., Ho, F. C. & Waldorf, A. Research on thin film anticounterfeiting coatings at the National Research Council of Canada. *Appl. Opt.* **28**, 2702–2717 (1989).
26. Granqvist, C. G. & Hjortsberg, A. Surfaces for radiative cooling: silicon monoxide films on aluminum. *Appl. Phys. Lett.* **36**, 139–141 (1980).
27. Raman, A. P., Anoma, M. A., Zhu, L., Rephaeli, E. & Fan, S. Passive radiative cooling below ambient air temperature under direct sunlight. *Nature* **515**, 540–544 (2014).
28. Chen, Z., Zhu, L., Raman, A. & Fan, S. Radiative cooling to deep sub-freezing temperatures through a 24-h day–night cycle. *Nat. Commun.* **7**, 13729 (2016).
29. Chen, D. Anti-reflection (AR) coatings made by sol–gel processes: a review. *Sol. Energy Mater. Sol. Cells* **68**, 313–336 (2001).
30. Li, Z., Butun, S. & Aydin, K. Large-area, lithography-free super absorbers and color filters at visible frequencies using ultrathin metallic films. *ACS Photonics* **2**, 183–188 (2015).
31. ElKabbash, M., Iram, S., Letsou, T., Hinczewski, M. & Strangi, G. Designer perfect light absorption using ultrathin lossless dielectrics on absorptive substrates. *Adv. Opt. Mater.* **6**, 1800672 (2018).
32. Kats, M. A., Blanchard, R., Genevet, P. & Capasso, F. Nanometre optical coatings based on strong interference effects in highly absorbing media. *Nat. Mater.* **12**, 20–24 (2012).

33. ElKabbash, M. et al. Iridescence-free and narrowband perfect light absorption in critically coupled metal high-index dielectric cavities. *Opt. Lett.* **42**, 3598–3601 (2017).
34. Svensson, J. S. E. M. & Granqvist, C. G. Electrochromic coatings for 'smart windows'. *Sol. Energy Mater.* **12**, 391–402 (1985).
35. Thielsch, R.in *Optical Interference Coatings* (eds Kaiser, N. & Pulker, H. K.) 257–279 (Springer, 2003).
36. *Optical Thin Films and Coatings, From Materials to Applications* 2nd edn (Elsevier, 2013).
37. Fan, S. Thermal photonics and energy applications. *Joule* **1**, 264–273 (2017).
38. Fann, C.-H. et al. Broadband infrared plasmonic metamaterial absorber with multipronged absorption mechanisms. *Opt. Express* **27**, 27917–27926 (2019).
39. ElKabbash, M. et al. Hydrogen sensing using thin-film perfect light absorber. *ACS Photonics* **6**, 1889–1894 (2019).
40. Sreekanth, K. V. et al. Generalized Brewster angle effect in thin-film optical absorbers and its application for graphene hydrogen sensing. *ACS Photonics* https://doi.org/10.1021/acsphotonics.9b00564 (2019).
41. Gallinet, B. in *Fano Resonances in Optics and Microwaves* (eds Kamenetskii, E. et al.) 109–136 (Springer, 2018).
42. Joe, Y. S., Satanin, A. M. & Kim, C. S. Classical analogy of Fano resonances. *Phys. Scr.* **74**, 259–266 (2006).
43. Ismail, N., Kores, C. C., Geskus, D. & Pollnau, M. Fabry-Pérot resonator: spectral line shapes, generic and related Airy distributions, linewidths, finesses, and performance at low or frequency-dependent reflectivity. *Opt. Express* **24**, 16366–16389 (2016).
44. Vorobyev, A. Y. & Guo, C. Colorizing metals with femtosecond laser pulses. *Appl. Phys. Lett.* **92**, 041914 (2008).
45. Fu, S. et al. Review of recent progress on single-frequency fiber lasers [Invited]. *J. Opt. Soc. Am. B* **34**, A49–A62 (2017).
46. Lee, K.-T., Ji, C., Banerjee, D. & Guo, L. J. Angular- and polarization-independent structural colors based on 1D photonic crystals. *Laser Photon. Rev.* **9**, 354–362 (2015).
47. Branz, H. M., Regan, W., Gerst, K. J., Borak, J. B. & Santori, E. A. Hybrid solar converters for maximum exergy and inexpensive dispatchable electricity. *Energy Environ. Sci.* **8**, 3083–3091 (2015).
48. Mojiri, A., Taylor, R., Thomsen, E. & Rosengarten, G. Spectral beam splitting for efficient conversion of solar energy—a review. *Renew. Sustain. Energy Rev.* **28**, 654–663 (2013).
49. Vossier, A. et al. Performance bounds and perspective for hybrid solar photovoltaic/thermal electricity-generation strategies. *Sustain. Energy Fuels* **2**, 2060–2067 (2018).
50. Maghanga, C. M., Niklasson, G. A., Granqvist, C. G. & Mwamburi, M. Spectrally selective reflector surfaces for heat reduction in concentrator solar cells: modeling and applications of TiO_2:Nb-based thin films. *Appl. Opt.* **50**, 3296–3302 (2011).
51. Wang, Y., Liu, H. & Zhu, J. Solar thermophotovoltaics: progress, challenges, and opportunities. *APL Mater.* **7**, 080906 (2019).
52. Sun, X., Sun, Y., Zhou, Z., Muhammad, A. & Bermel, P. Radiative sky cooling: fundamental physics, materials, structures, and applications. *Nanophotonics* **6**, 997–1015 (2017).
53. Singh, S. C. et al. Solar-trackable super-wicking black metal panel for photothermal water sanitation. *Nat. Sustain*. https://doi.org/10.1038/s41893-020-0566-x (2020).
54. Denholm, D., O'Connell, M., Brinkman, G. & Jorgenson, J. *Overgeneration from Solar Energy in California: A Field Guide to the Duck Chart* (National Renewable Energy Laboratory, 2015).
55. Sreekanth, K. V. et al. Phase-change-material-based low-loss visible-frequency hyperbolic metamaterials for ultrasensitive label-free biosensing. *Adv. Opt. Mater.* **7**, 1900081 (2019).
56. Zhan, Z. et al. Enhancing thermoelectric output power via radiative cooling with nanoporous alumina. *Nano Energy* **65**, 104060 (2019).
57. Kraemer, D. et al. High-performance flat-panel solar thermoelectric generators with high thermal concentration. *Nat. Mater.* **10**, 532–538 (2011).
58. Jalil, S. A. et al. Spectral absorption control of femtosecond laser-treated metals and application in solar-thermal devices. *Light. Sci. Appl.* **9**, 14 (2020).
59. Xu, Y. & Miroshnichenko, A. E. Reconfigurable nonreciprocity with a nonlinear Fano diode. *Phys. Rev. B* **89**, 134306 (2014).
60. Chen, Z. et al. Graphene controlled Brewster angle device for ultra broadband terahertz modulation. *Nat. Commun.* **9**, 4909 (2018).

Publisher's note Springer Nature remains neutral with regard to jurisdictional claims in published maps and institutional affiliations.

© The Author(s), under exclusive licence to Springer Nature Limited 2021

Methods

Coupled oscillator theory of FROCs. Here, we detail the coupled oscillator model presented in the manuscript. We considered the two resonators defined earlier: an externally driven oscillator with large damping (resonator 1) that is weakly coupled to a less damped oscillator (resonator 2).

To allow for the analytical results presented in equations (1)–(3), we made several simplifications. (1) All fields in are assumed to be propagating along the normal incidence direction (parallel or antiparallel). (2) Although the refractive indices in principle depend on the angular frequency of light ω, our focus is on a narrow range of frequencies around resonance, and we ignore the dispersion of the indices within this range. Incorporating the dispersion into the theory would change the quantitative details, but not the qualitative results. (3) The coupling between the resonators occurs through the component of the field that leaks from resonator 1 through the metal into resonator 2. We worked in the weak coupling regime, in which the metal layer is assumed thick enough that most of the field is attenuated in passing through the metal. Specifically, we assume that $L_m \gg c/(\omega n_m^{Im})$.

To formulate the theory, it was useful to refer to the complex Fresnel reflection and transmission coefficients at various interfaces. These are indicated by r_{ij} and t_{ij}, respectively, in Fig. 1b, where i is the material in which the field originates, and j is the material in which the field is transmitted. The coefficients can be expressed in terms of the refractive indices of the respective materials:

$$r_{ij} = \frac{n_i - n_j}{n_i + n_j}, \quad t_{ij} = \frac{2n_i}{n_i + n_j}. \tag{4}$$

For convenience, we decided to treat the metal spacer layer as an effective interface between the lossy material and the dielectric. The associated reflectance and transmission coefficients are indicated with tildes and have a more complicated form than a simple interface between two materials. For fields within the lossy material propagating into the dielectric through the metal, the coefficients are:

$$\tilde{r}_{ad} = \frac{(n_a + n_m)(n_m - n_d) + e^{-2i\phi_m(\omega)}(n_a - n_m)(n_m + n_d)}{(n_a - n_m)(n_m - n_d) + e^{-2i\phi_m(\omega)}(n_a + n_m)(n_m + n_d)} \approx \frac{n_a - n_m}{n_a + n_m} = r_{am}; \tag{5}$$

$$\tilde{t}_{ad} = \frac{4n_d n_m e^{-i\phi_m(\omega)}}{(n_d - n_m)(n_m - n_a) + e^{-2i\phi_m(\omega)}(n_a + n_m)(n_m + n_d)} \approx \frac{4n_d n_m e^{i\phi_m(\omega)}}{(n_a + n_m)(n_m + n_d)}. \tag{6}$$

Here, $\phi_i(\omega) \equiv n_i L_i \omega/c$ is the (possibly complex) phase gained by passing through a material of index n_i and thickness L_i. We have used the weak coupling assumption (point 3 above) to give simpler approximate forms on the right, keeping the leading order contributions. Note that the reflection coefficient is approximately the same as from a simple metal interface, r_{am}. For the transmission coefficient, as L_m increases, $e^{i\phi_m(\omega)} \propto e^{-n_m^{Im} L_m \omega/c} \to 0$, and hence the coefficient becomes progressively attenuated, consistent with the weak coupling assumption. Analogously, for fields within the dielectric propagating upwards into the lossy material through the metal,

$$\tilde{r}_{da} \approx \frac{n_d - n_m}{n_d + n_m} = r_{dm}, \quad \tilde{t}_{da} \approx \frac{4n_a n_m e^{i\phi_m(\omega)}}{(n_d + n_m)(n_a + n_m)}. \tag{7}$$

To set up our theoretical description, we first considered each resonator separately, uncoupled from the other. It was easier to start with resonator 2, the MDM Fabry-Pérot cavity. Imagine a field E_{2i} that was injected at the top of the lossless dielectric, propagating downwards. The total field E_2 that establishes itself in the cavity is the sum of this original field and an infinite series of reflections from the bottom and top metallic interfaces:

$$E_2 = E_{2i} + E_{2i}\, r_{dm}\tilde{r}_{da} e^{2i\phi_d(\omega)} + E_{2i} r_{dm}^2 \tilde{r}_{da}^2 e^{4i\phi_d(\omega)} + \ldots \tag{8}$$

Summing these reflections, we can express the ratio of the total to the injected field as:

$$\frac{E_2}{E_{2i}} = \frac{1}{1 - r_{dm}\tilde{r}_{da} e^{2i\phi_d(\omega)}} \equiv A_2(\omega) \tag{9}$$

Using the fact that $\tilde{r}_{da} \sim r_{dm}$, as discussed above, and writing the complex coefficient $r_{dm} = |r_{dm}| e^{i\phi_{dm}}$ in terms of amplitude and phase, we can rewrite the ratio $A_2(\omega)$ in the form:

$$A(\omega) \approx \frac{1}{1 - |r_{dm}|^2 e^{2i[\phi_d(\omega) + \phi_{dm}]}}$$

This cavity exhibits resonance at frequencies ω_2 defined by the condition $\phi_d(\omega_2) = -\phi_{dm} + k\pi$, where k is some integer. Using the definition of r_{dm} from equation (1), we can also express this condition as:

$$\tan\phi_d(\omega_2) = \tan\phi_{dm} = \frac{2n_d n_m^{Im}}{n_d^2 - (n_m^{Im})^2 - (n_m^{Re})^2} \tag{10}$$

For frequencies ω in the vicinity of the resonant value ω_2, we can Taylor expand the denominator of equation (6) and write the ratio of field intensities $|A_2(\omega)|^2$ in an approximate damped resonant oscillator form:

$$|A_2(\omega)|^2 \approx \frac{c^2}{4n_d^2 L_d^2 |r_{dm}|^2}\left[\frac{1}{\Gamma_2^2 + (\omega - \omega_2)^2}\right], \tag{11}$$

where the damping factor Γ_2 is given by

$$\Gamma_2 = \frac{c(1 - |r_{dm}|^2)}{2n_d L_d |r_{dm}|} \approx \frac{2cn_m^{Re}}{L_d\left[n_d^2 + (n_m^{Im})^2\right]}. \tag{12}$$

Here, we have approximated the expression using the assumption $n_m^{Re} \ll n_m^{Im}$ for the metal, keeping the leading order contribution to Γ_2. As we approach the ideal metal limit, $n_m^{Re} \to 0$, the damping factor Γ_2 vanishes. But for any real metal there will be some finite damping in the MDM cavity. Figure 1c shows an example of $|A_2(\omega)|^2$ versus ω for the following sample material parameters: $n_0 = 1$, $n_m = 0.01 + 4i$, $n_a = 2.2 + 0.5i$, $n_d = 2.5$, $L_m = 35$ nm, $L_a = 40$ nm and $L_d = 70$ nm. In addition to the intensity, one can characterize the phase $\Phi_2(\omega)$ of the resonator, defined by $A_2(\omega) = |A_2(\omega)| e^{i\Phi_2(\omega)}$. Figure 1d shows $\Phi_2(\omega)$ making a sharp switch from negative to positive as ω passes through resonance. In the undamped limit, this phase difference would have magnitude π, but with finite damping it is always less than π.

Then, we considered resonator 1 alone. We proceeded analogously, calculating the total field E_1 that is established in the lossy material when a field E_{1i} is injected. For the uncoupled resonator we assumed the reflection coefficient from the bottom is just r_{am}, a simple interface between the lossy material and metal. The ratio of the total to the injected field is then:

$$\frac{E_1}{E_{1i}} = \frac{1}{1 - r_{a0} r_{am} e^{2i\phi_a(\omega)}} \equiv A_1(\omega). \tag{13}$$

Writing $r_{a0} = |r_{a0}| e^{i\phi_{a0}}$, $r_{am} = |r_{am}| e^{i\phi_{am}}$, we can rewrite the above equation in the form given by equation (1) in the text:

$$A_1(\omega) = \frac{1}{1 - |r_{a0} r_{am}| e^{i[2\phi_a(\omega) + \phi_{a0} + \phi_{am}]}}, \tag{14}$$

which can be rewritten as

$$A_1(\omega) = \frac{1}{1 - |r_{a0} r_{am}| e^{-2Im[\phi_a(\omega)]} e^{i\{2Re[\phi_a(\omega)] + \phi_{a0} + \phi_{am}\}}}, \tag{15}$$

where $Re[\phi_a(\omega)] = n_a^{Re} L_a \omega/c$ and $Im[\phi_a(\omega)] = n_a^{Im} L_a \omega/c$. There is no exact analytical expression for the frequency ω_1 at which $A_1(\omega)$ exhibits resonance. However, under the assumption that n_a^{Im} is typically smaller than n_a^{Re}, the resonant frequency is given by the following approximate condition: $2Re[\phi_a(\omega_1)] \approx -\phi_{a0} - \phi_{am} + 2k\pi$, where k is an integer.

As with the earlier case, we can express the ratio of intensities in the form of a damped, resonant oscillator. Using the above approximation, we have

$$|A_1(\omega)|^2 = \frac{c^2 e^{2n_a^{Im} L_a \omega_1/c}}{4(n_a^{Re})^2 L_a^2 |r_{am} r_{a0}|}\left(\frac{1}{\Gamma_1^2 + (\omega - \omega_1)^2}\right), \tag{16}$$

where the damping factor Γ_1 is given by

$$\Gamma_1 = \frac{c e^{n_a^{Im} L_a \omega_1/c}\left(1 - e^{-2n_a^{Im} L_a \omega_1/c}|r_{am} r_{a0}|\right)}{2n_a^{Re} L_a |r_{a0} r_{am}|^{1/2}}. \tag{17}$$

Unlike resonator 2, for which one could approach the undamped limit as the metal becomes ideal ($\Gamma_2 \to 0$ as $n_m^{Re} \to 0$), here it is generally not possible to eliminate the damping. This is unsurprising, because unlike the Fabry-Pérot cavity, we only have a metallic mirror at one surface and a lossy medium. For Γ_1 to vanish, the product of $e^{-2n_a^{Im} L_a \omega_1/c}$, $|r_{am}|$ and $|r_{a0}|$ in the numerator would have to equal 1. Because each of these terms is ≤ 1, that would mean each term individually would have to approach 1 for Γ_1 to become zero. Eliminating losses in the medium, $n_a^{Im} \to 0$, and making the metal at the bottom ideal, $n_m^{Re} \to 0$, would make the first and third terms equal to 1, respectively. However, in this limiting case, $|r_{a0}| \to |n_0 - n_a^{Re}|/|n_0 + n_a^{Re}|$, which is always less than 1 for real materials. So Γ_1 would still be non-zero. This highlights the fact that resonator 1 will in general

be more strongly damped than resonator 2, that is, $\Gamma_1 > \Gamma_2$, and one can readily arrange parameters such that $\Gamma_1 \gg \Gamma_2$. An example of this is shown in Fig. 1c, in which the resonance of $|A_1(\omega)|^2$ is highly damped compared with that of $|A_2(\omega)|^2$. The corresponding phase $\Phi_1(\omega)$, shown in Fig. 1d, shows a gradual crossover from negative to positive near ω_1, in contrast to the sharp change in $\Phi_2(\omega)$ for the less damped resonator.

Finally, we considered what happens when we couple the two resonators together and drive the strongly damped resonator 1. This drive comes from the incident field E_i in the superstrate, which contributes $t_{0a}E_i$ to the field injected into resonator 1. However, there is another contribution from the field in resonator 2 that is reflected upwards from the metal substrate through the metal spacer layer into resonator 1. We can express the total field injected into resonator 1 as $E_{1i} = t_{0a}E_i + E_2 r_{dm} r_{a0} \tilde{t}_{da} e^{i[2\phi_d(\omega)+\phi_a(\omega)]}$. In turn, the fact that there exists a field in resonator 2 is due to the field from resonator 1 propagating downwards through the metal spacer, given by $E_{2i} = E_1 \tilde{t}_{ad} e^{i\phi_a(\omega)}$. All these relationships can be succinctly expressed through equation (3) in the manuscript.

The coupling between E_1 and E_2 occurs through the two off-diagonal terms in the matrix of equation (3), which are assumed small under our weak coupling assumption. In fact, as the spacer metal layer thickness becomes large, $L_m \to \infty$, the transmission coefficients across the spacer, $\tilde{t}_{da}$ and $\tilde{t}_{ad}$, vanish, making the coupling terms zero. In this limit we recover the two uncoupled oscillators discussed above. For finite L_m, we have all the ingredients necessary for Fano resonance: a strongly damped, driven oscillator (resonator 1) weakly coupled to a less damped oscillator (resonator 2). Indeed, the form of equation (3) is similar in structure to the simple two-oscillator description of Fano resonance given in ref. [1]. Following the approach in ref. [1] the Fano parameter q can be approximately related to the degree of detuning δ between the two oscillators at the resonant frequency of the less damped one: $q \approx \cot\delta$, where $\delta = \Phi_1(\omega_2)$. To observe the Fano resonance near ω_2, one can look at the reflected field E_r in the superstrate (from which one derives the reflectance $R = |E_r / E_i|^2$), which has contributions from the reflections of both E_i and E_2:

$$E_r = r_{0a}E_i + r_{am}t_{a0}e^{2i\phi_a(\omega)}E_1 + r_{dm}\tilde{t}_{da}t_{a0}e^{i[2\phi_d(\omega)+\phi_a(\omega)]}E_2 \tag{18}$$

Beam splitter filter theoretical analysis. Here, we considered what occurs in the beam splitter configuration when we replaced the metal substrate at the bottom of the FROC with a metal layer of thickness L_m and used a dielectric substrate of refractive index n_s. We obtained a field E_t transmitted into the substrate due to leakage of E_2 through the bottom metal layer: $E_t = \tilde{t}_{ds}e^{i\phi_d(\omega)}E_2$. Here, $\tilde{t}_{ds}$ is given by equation (7) with n_a replaced by n_s. The resonance in E_2 at ω_2 thus translates into a peak in E_t near the same frequency. We thus observe beam splitter behaviour with peaks in both reflectance R and transmittance $T = (n_s/n_0)|E_t/E_i|^2$ near ω_2. This is illustrated in Supplementary Fig. 17 with the same sample material parameters as mentioned above and $n_s = 1.5$.

Sample fabrication. Films were deposited on a glass substrate (Micro slides, Corning) using electron-beam evaporation for Ni (5 Å s^{-1}), Ge (3 Å s^{-1}), TiO_2 (1 Å s^{-1}) and MgF_2 (5 Å s^{-1}) pellets and thermal deposition for Au (10 Å s^{-1}) and Ag (20 Å s^{-1}), with the deposition rates specified for each material. All materials were purchased from Kurt J. Lesker.

Numerical calculation of the reflection and absorption spectra. Numerical reflection and absorption spectra were generated using a transfer matrix-based simulation model written in Mathematica[61]. The power dissipation distribution in the thin-film stack was calculated using the commercially available finite-difference time-domain (FDTD) software from Lumerical[62]. The simulation was performed using a two-dimensional model with incident plane wave at zero incidence angle. Periodic boundary conditions were used in the x direction and perfectly matched layers were used in the y direction (normal to the sample). The mesh was tailored to each layer with a mesh step of 0.001 µm. Absorption is complementary to the calculated reflection and transmission, that is, $A = 1 - R - T$, and is complementary to the reflectance for opaque substrates.

Angular reflection measurements. Angular reflection was measured using a variable-angle high-resolution spectroscopic ellipsometer (Woollam, V-VASE). The transmittance was zero for all wavelengths and angles.

Bandwidth and resonance wavelength of FROC reflection line. The broadness of the observed Fano resonance can be tuned and made sharper. The broadness of the FROC resonance depends on the damping factor of the weakly damped cavity Γ_2 (equation (12)). For a non-zero incidence angle, this can be generalized to yield the reflection line bandwidth $\delta\lambda$ for an MDM Fabry-Pérot cavity, which is given by $\delta\lambda = \lambda_0^2(1-R)/(2n_dL_d\cos\theta\pi\sqrt{R})$, where λ_0 is the peak wavelength, R is reflectance, n_d and L_d are the dielectric index and thickness, respectively, and θ is the incidence angle. Accordingly, to optimize the bandwidth, the mirror reflectance, the dielectric optical thickness and incident angle should increase.

Furthermore, using the transfer matrix method, we could determine the dielectric thickness necessary to realize a resonant reflection line at a given wavelength λ. We considered a FROC containing a lossless dielectric with refractive index $n_d(\lambda)$ and thickness L_d. The surrounding metal layers have index $n_m(\lambda) + ik_m(\lambda)$, and we assumed $n_m \ll k_m$ (which is true for Ag in the wavelength range of interest). The condition for resonance in the FROC is:

$$\tan\left[\frac{2\pi n_d(\lambda)L_d}{\lambda}\right] = \frac{2k_m(\lambda)n_d(\lambda)}{n_d^2(\lambda) - k_m^2(\lambda)} \tag{19}$$

Given L_d, one can numerically try to solve this condition to find λ. Alternatively, if λ is specified, the above equation can be solved for L_d:

$$L_d = \frac{\lambda}{2\pi n_d(\lambda)}\left\{m\pi - \tan^{-1}\left[\frac{2n_d(\lambda)k_m(\lambda)}{k_m^2(\lambda) - n_d^2(\lambda)}\right]\right\} \tag{20}$$

Here, m is an integer. Note that the condition for L_d is independent of the details of the Ge layer on top, or the thickness of the metal, as long as the assumptions of Fano resonance are satisfied, that is, the MDM FWHM << the broadband absorption continuum.

Iridescence properties of FROCs. The iridescence of a FROC's resonant reflection mode depends entirely on the properties of the MDM cavity. The dependence of the reflection peak wavelength λ_{max} on the incident angle is thus given by[33]:

$$\frac{1}{\lambda_{max}(\theta)}\frac{d\lambda_{max}(\theta)}{d\theta} \sim H[\lambda_{max}(\theta), \theta, n_d]\frac{\cos\theta\sin\theta}{n_d^2 - \sin^2\theta}, \tag{21}$$

where $H[\lambda_{max}(\theta), \theta, n_d]$ is a dimensionless function that depends solely on θ through λ_{max}. As n_d increases to values $\gg 1$, the above expression decreases as n_d^{-2}. Accordingly, the iridescence of FROCs can be mitigated by using a high-index dielectric.

Calculating the average spectral absorptance and emissivity. The spectrally averaged absorptivity of the selective surface is given by[63]:

$$\bar{\alpha} = \frac{1}{I}\int_0^\infty d\lambda\varepsilon(\lambda)\frac{dI}{d\lambda} \tag{22}$$

And the emissivity is given by:

$$\bar{\varepsilon} = \frac{\int_0^\infty d\lambda\varepsilon(\lambda)/\{\lambda^5[\exp(hc/\lambda kT) - 1]\}}{\int_0^\infty d\lambda/\{\lambda^5[\exp(hc/\lambda kT) - 1]\}}, \tag{23}$$

where I is the solar intensity, λ is the wavelength, $\varepsilon(\lambda)$ is the spectral emissivity of the selective absorber/emitter, $\frac{dI}{d\lambda}$ is the spectral light intensity, which corresponds to the AM 1.5 solar spectrum, h is Planck's constant, c is the speed of light, k is Boltzmann's constant and T is the absorber temperature, here taken as 100 °C.

Photovoltaic measurements. A solar simulator (Sanyu) with an AM1.5G airmass filter was first calibrated for 1 Sun (1,000 W m^{-2}) using an NREL-certified PV reference solar cell (PV Measurements). The measured power of a thermopile power meter (FieldMax II TO, Coherent; minimum measurable power ±10 µW) was set to a wavelength of 500 nm, corresponding to 1,000 W m^{-2} from the calibrated solar simulator and was used as unit of one optical concentration. A plano-convex lens of 250 mm focal length and 150 mm diameter was mounted at the output port of the solar simulator to enhance optical concentration. The simulator current was varied to adjust solar irradiance from 1,000 W m^{-2} (286 mW at thermopile head) to 5,000 W m^{-2} (1,430 mW). The PV cell was purchased, cut and two wires were soldered to create a functioning PV cell. The temperature was measured using thermocouples (temperature accuracy ±1 °C) and we have reported the equilibrium temperature. Power was measured using a Keithley 2400 source meter using an open circuit voltage and sweeping the voltage down to zero while measuring the current. The maximum power reported is the maximum of the voltage and current product.

Data availability

The raw numerical data for the figures in the manuscript, as well as the code on the thin-film coupled oscillator theory, are available via GitHub at https://github.com/hincz-lab/Fano-resonant-ultrathin-film-optical-coatings-FROC.

References

61. Mathematica v.12 (Wolfram, 2019).
62. Lumerical (Ansys, Inc., 2020).
63. Bermel, P. et al. Design and global optimization of high-efficiency thermophotovoltaic systems. *Opt. Express* **18**, A314–A334 (2010).

Acknowledgements

We thank M. Mann and J. A. Fenster for their assistance in taking high-quality photos. We thank H. M. Cao for providing assistance in schematics. M.E. acknowledges fruitful

discussions with K. Singer. C.G. acknowledges the support of the Army Research Office, the National Science Foundation and AlchLight. G.S. and M.H. acknowledge the support of the National Science Foundation.

Author contributions

M.E., C.G., G.S. and M.H. discussed and defined the project. C.G., G.S. and M.H. supervised the research. M.E. developed the approach and initiated the project. T.L., S.A.J., C-H.F. and M.E. fabricated the samples. M.E., T.L., J.R., S.A.J. and N.H. performed the experiments. M.H. developed the coupled oscillator theory. M.E. and J.Z. performed FDTD simulations. M.E. wrote the manuscript with input from all the authors. All authors discussed the results.

Competing interests

A patent application has been filed on the Fano resonance optical coating scheme in this work.

Additional information

Supplementary information is available for this paper at https://doi.org/10.1038/s41565-020-00841-9.

Correspondence and requests for materials should be addressed to M.E., M.H., G.S. or C.G.

Peer review information *Nature Nanotechnology* thanks Koray Aydin and Jiming Bao for their contribution to the peer review of this work.

Reprints and permissions information is available at www.nature.com/reprints.

View publication stats